This is the Pre-Published Version.

This is the Author Manuscript of the work. The final published article is available at https://doi.org/10.1680/jstbu.16.00182.

The following publication Zhu, J. Y., & Chan, T. M. (2018). Behaviour of polygonal-shaped steel-tube columns filled with high-strength concrete. Proceedings of the Institution of Civil Engineers-Structures and Buildings, 171(2), 96-112 is available at https://doi.org/10.1680/jstbu.16.00182.

Behaviour of high-strength CFST polygonal shaped stub columns

Jiong-Yi ZHU, Tak-Ming CHAN*

Department of Civil and Environmental Engineering, The Hong Kong Polytechnic University, Hung Hom, Hong Kong SAR

*tak-ming.chan@polyu.edu.hk

Abstract

This paper presents an investigation on axially loaded concrete filled steel tubes (CFST) with different polygonal cross-sections including triangular, hexagonal and octagonal shapes. The nominal concrete compressive cylinder strength adopted was 100 MPa and the nominal yield strength of the steel was 285 MPa. For each cross-sectional shape, two identical specimens of CFST and one specimen of a complementary hollow steel tube were examined. Load-shortening/strain histories and failure modes were recorded and compared. Finite element analysis with three different existing constitutive models of concrete were also developed and validated against the experimental results. The load carrying capacity of the CFST were compared with the derived values in current design documents including BS EN 1994-1-1:2004, ACI 318-11/AISC 360-16 and GB50936-2014. The feasibility of current design documents on CFST with different types of cross-section was discussed.

Keywords

Concrete filled steel tubes; Polygonal cross-section shape; High strength concrete; Load capacity; Ductility; Finite element model; Composite column design.

List of notations

A_c	cross-section area of concrete core
A_s	cross-section area of steel tube
A_{sc}	cross-section area of CFST
B	width of square cross-section
D	measured width defined in Figure 2 or diameter of circular section
D_{eq}	equivalent diameter
DI	ductility index
DI_{FE}	ductility index from FE analysis
E_c	elastic modulus of concrete
E_{c2}	descending modulus of concrete in post-peak stage
E_s	elastic modulus of steel
ε	uniaxial strain of confined concrete
$\varepsilon_{85\%}$	uniaxial strain when the load decreases to 85% of ultimate load
ε_{cc}	uniaxial strain at peak stress of confined concrete
ε_{co}	uniaxial strain of unconfined concrete
ε_f	elongation at fracture based on the original gauge length
ε_u	axial strain at ultimate load
f_{bo}/f_{co}	strength ratio of concrete between biaxial compression and uniaxial compression
f_{cc}	peak stress of confined concrete
f_{co}	cylinder strength of concrete core
$f_{co,cube}$	cube strength of concrete
f_l	confining pressure
f_{sc}	strength of CFST
f_{re}	residual stress of confined concrete
f_y	yield stress of the virgin steel plate
K	the ratio of the second stress invariant on the tensile meridian to that on the compressive meridian

N_{cr}	elastic critical force
N_d	load capacity from code of practice
N_u	load capacity of specimen
$N_{u,\,CFST}$	load capacity of CFST
$N_{u,\,FE}$	prediction of load capacity in FE analysis
$N_{u,\,tube}$	load capacity of hollow steel tube
P	perimeter of the cross-section
S_o	cross-section area of tensile coupon
t	thickness of steel tube
$\delta_{u,tube}$	axial shortening of hollow steel tube at peak load
$\delta_{u,CFST}$	axial shortening of CFST at peak load
$\delta_{u,\,FE}$	predicted axial shortening at peak load in FE analysis
ξ	confinement ratio equal to $A_s f_y / A_c f_{co}$
σ	uniaxial stress of confined concrete
$\sigma_{0.2}$	0.2% proof stress of hollow steel tube
$\sigma_{0.2\text{-}t}$	0.2% proof stress of tensile coupon
σ_u	ultimate stress of tensile coupon
Ψ	dilation angle
ω	local imperfection of steel tube

1. Introduction

Concrete filled steel tubes (CFST) are widely used as columns in modern construction due their high load carrying capacity and ductility. These highly efficient structural members have attracted significant attention from researchers in the last six decades. Kloppel and Goder (1957) presented the earliest experimental studies on CFST, after that numerous experimental studies were conducted to investigate the compressive behaviour of CFST focusing on a range of parameters including cross-section shapes, diameter to width ratios D/t and concrete grades (e.g. Furlong 1967, Tomii et al.1977, Schneider 1998, O'Shea and Bridge 2000, Han 2002, Giakoumelis and Lam 2004, Liew

and Xiong 2010, Evirgen et al. 2014, Ren et al. 2014).

Circular and rectangular cross-sections are the two most commonly used cross-sections in practical design. The confinement effect of CFST with rectangular cross-section is limited compare to its circular counterpart. However, the column size of CFST with circular cross-section may reduce the lettable flooring area of a building. Therefore, to strike a balance between structural efficiency and optimized floor area, a wider range of cross-sectional shapes should be adopted for the design of CFST columns.

Schneider (1998) investigated the experimental behaviour of CFST with circular and rectangular cross-section shapes under concentric load. Fourteen specimens were tested and the test results indicated that the circular CFST shows more ductility in post yielding behaviour than the square and rectangular CFST shapes. A similar observation was made by Han (2002), when experimental research on rectangular CFST was undertaken. Twenty-four specimens with various confinement ratios, ξ and geometric properties were tested. It was concluded that the confinement ratio and geometric properties have a significant influence on the load-carrying capacity and ductility of rectangular CFST. Tomii et al. (1977) considered octagonal cross-section shapes, in CFST experimental study. Sixty specimens with octagonal cross-section shape were tested. In their experiments, the strain hardening or elastic-perfectly-plastic relation was found in circular and octagonal columns and degrading curves were observed in square columns. Tomii et al. (1977) concluded the confinement effect can be anticipated in circular and octagonal CFST, however the load capacity of square CFST would not be improved by the triaxial effect. The effect of confinement was further studied by Susantha et al. (2001). They investigated the lateral confining pressure on circular, square and octagonal CFST. It was found that the most efficient confinement was obtained from circular CFST while the square CFST has a negligible confinement effect, and the octagonal CFST has a moderate confinement compared with the circular and square CFST shapes. They also indicated that the confinement effect was also affected by the D/t ratio and the concrete and steel strengths.

Recently, more studies on polygonal CFST were undertaken. Yu et al. (2013) proposed a unified formula for the load capacity of polygonal CFST and validated the formula by the existing experimental studies. Evirgen et al. (2014) tested 64 CFST specimens with circular, hexagonal, rectangular and square cross-sections. The test results indicated that the circular CFST has the most efficient load capacity and ductility. Ren et al. (2014) conducted experimental studies on CFST with special-shaped cross-sections which covered triangular, fan-shaped, D-shaped, 1/4 circular and semi-circular cross-section shapes. The results showed that the failure mode of these types of CFST was similar to that of square CFST. An experimental programme of testing on hexagonal CFST was carried out by Xu et al. (2016), and it was indicated that out-of-plane local buckling was the main failure mode in their tests. The above studies have indicated the importance of cross-section shape on the axial behavior of CFST especially on the softening behaviour, but a comparative study on the polygonal cross-sections such as triangular, hexagonal and octagonal have not been conducted yet.

The use of high strength concrete is efficient in improving the structural behavior of columns due to its high strength and high stiffness especially in high-rise buildings. Giakoumelis and Lam (2004) conducted a test programme of 15 CFST specimens with concrete strengths of 30 MPa, 60 MPa, and 100 MPa. The test results indicated that the increase of concrete strength would affect the bond strength between the steel tube and the concrete core. Liew and Xiong (2010) conducted a test on ultra-high strength concrete (UHSC) filled steel tubes with a concrete strength of 200 MPa. The results indicated that the post-peak behavior of UHSC filled steel tubes is brittle especially when the confinement ratio ξ is low. However most of the existing literature for high strength concrete filled steel tubes focused on the cross-section shapes of circular and rectangular.

Based on a critical review of the existing studies, this paper presents an investigation

including physical tests and finite element analyses to study the axial behaviour of high strength CFST with triangular, hexagonal and octagonal cross-sections. The impact of cross-section shape on the load capacity and ductility of these CFST sections was discussed. The outcomes of the experimental studies were also used in the assessment of existing design provisions in European, American, and Chinese Standards.

2. Experimental investigation

2.1 Specimens and geometric measurements

In the present study, three hollow steel tubes and six high strength concrete filled steel tubes (CFST) with triangular, hexagonal, and octagonal cross-section shapes and with a measured cylinder compressive strength of 100 MPa, for the concrete were tested under monotonic axial compression. Steel tubes with octagonal and hexagonal cross-section shapes were fabricated by welding two cold-formed 3 mm thick steel plates, bent to form a half-section as shown in Figure 1 Steel tubes with triangle cross-section shape were fabricated by directly welding three steel plates together as shown in Figure 1(c). Specimens were labelled as X-Y-Z. X indicates the cross-section shape of the specimens where T stands for triangular, H stands for hexagonal and O stands for octagonal. Y indicates the column types where H stands for hollow tubes and CF stands for CFST. Z is used to differentiate two nominally identical specimens. The dimensions of the cross-section for each specimen were precisely measured using a digital caliper with an accuracy of 0.01 mm. Table 1 shows the averaged value of the measured width D as shown in Figure 2 of all the test specimens and the corresponding tube thickness and height.

The geometric local imperfection in terms of deviation from a plane surface for all the specimens was measured over the height of each specimen before the compression test. Figure 3 shows the arrangement of the measurement. The specimen was placed on a milling machine which can move horizontally. A dial gauge with a tolerance of 0.01 mm was used to measure the local imperfection at mid-portion of each face with an interval of 30 mm over the height of the steel tubes. For the faces containing the welded

joints, the surface measurement location was near the mid-portion due to the roughness of the welding zone. The initial readings at both ends of the specimen were regarded as reference points and other readings were adjusted in relation to the reference points to eliminate the error from the initial tilting of the tube. Figure 4 shows that the measured imperfection profile for specimens T-H-1, H-H-1 and O-H-1. The figure shows the maximum imperfection of specimens H-H-1 and O-H-1 was found at the welding surface which indicated that the welding process can have significant impact on the magnitude of geometric local imperfections. Table 1 shows the maximum local imperfection for each specimen, including the ratios between the maximum imperfection and tube thickness.

2.2 Material test

2.2.1 Steel

Tensile coupon tests were conducted to obtain the material properties of the steel tubes. In this investigation, only flat tensile coupons from the virgin plates were tested. The dimensions of the steel coupon were established according to the BS EN ISO 6892-1 (2009). Figure 5 shows the dimensions of the steel coupons. Coupons were tested using a Testomeric M-500 testing machine with a load capacity of 50 kN. Strain gauges were attached at each side of the coupon to measure the strain at the initial stage (elastic stage) of the test. The Pixel method (Liu and Chung, 2016) was then used to obtain the elongation of the coupons after the tensile strain exceeded the limit of the strain gauge in the strain hardening stage. A high-megapixel digital camera with 12 megapixels was used to capture the elongation between the red marks on the tensile coupons as shown in Figure 6 via counting the pixels between the marks. Figure 7a shows how the data from the strain gauge and the Pixel method compared. The limit of the strain gauge is approximate 5%, after 5% strain, the strain measured by the pixel method was adopted. Table 2 shows the result of the tensile coupon test, where E_s is the elastic modulus of steel; $\sigma_{0.2}$ is the 0.2% proof stress; σ_u is the ultimate tensile stress and ε_f is the elongation at fracture based on the original gauge length of 30 mm, which is defined by BS EN

ISO 6892-1 (2009) as $5.65\sqrt{S_o}$, where S_o is the cross-sectional area of the tensile coupon. The static stress-strain curve was obtained by pausing the test for 100 seconds at 0.2% proof stress and at the ultimate stress (Huang and Young, 2014). The loading rate used in the tensile coupon test was 0.04% per min in tensile strain up to the $\sigma_{0.2}$ limit and 0.7% per min after that. This load rate agreement was adopted from the test procedure described by Huang and Young (2014). Figure 7b shows the static stress-strain curves for all the tensile coupons and also an idealized stress-strain curve which was generated for the numerical investigation.

2.2.2 Concrete

The high strength concrete was prepared with a water-to-cement ratio of 0.25. Table 3 shows the mix proportions at the saturated surface dry (SSD) condition. Five concrete cylinders, each with a diameter of 150 mm and a height of 300 mm, and five concrete cubes of 150 mm were cast and cured in moist conditions for at least 28 days as shown in Figure 8. The material properties of concrete were established from the compressive tests on the standard concrete cubes and cylinders at the test date of the CFST specimens. Four strain gauges with a gauge length of 100 mm were attached to the surface of the standard cylinders at 90^o to each other. Load control was adopted in testing the concrete cubes with a loading rate of 6 MPa/min and displacement control was used for the concrete cylinders tests with a rate of 0.18 mm/s. The test results are summarised in Table 4. It should be noted that the failure modes of cylinder 1 and cylinder 2 did not satisfy the recommended failure mode in BS EN 12390-3 (2009) and therefore the mean result is calculated from cylinder 3 to cylinder 5 only.

2.3 Stub column tests

Stub column tests were conducted under uniaxial compression conditions using an MTS machine with a load capacity of 5000 kN. Strain gauges were attached at mid-height of the specimens longitudinally and horizontally after the surface of the tube was carefully polished. Three to four linear variable differential transducers (LVDTs) with

an accuracy of 0.01 mm were installed around the specimens to record the axial shortening. Figure 9 shows the arrangement of the strain gauges and LVDTs for stub columns with triangular, hexagonal and octagonal cross-section shapes. Figure 10 shows the set-up of the uniaxial compression test. A similar set-up was also adopted by Chan et al. (2015). The loading rate for the stub columns was maintained at 0.3 mm/min. For stub columns with a hollow section, the test was paused for 100 s near the 0.2% proof stress and the ultimate stress to obtain static stress-strain curves which are compatible with the results from the tensile coupon test.

The test result for the hollow steel tubes is summarized in Table 5, where the $N_{u,tube}$ is the load capacity of the specimen and $\delta_{u,tube}$ is the axial shortening at the peak load. The axial load-shortening curves are also displayed in Figure 11. As shown in Table 5, a simple ductility index, *DI*, is used to quantify the ductility of specimens which is adopted from the referenced studies (Tao et al. 1998; Han et al. 2002). The ductility index is defined as follows:

$$DI = \frac{\varepsilon_{85\%}}{\varepsilon_u} \tag{1}$$

where ε_u is the axial strain at the ultimate load and $\varepsilon_{85\%}$ is the axial strain when the load decreases to 85% of the ultimate load. The 0.2% proof stress was compared with that from tensile coupons where the subscript *t* is for the result of a tensile coupon test (i.e. $\sigma_{0.2\text{-}t}$). It is apparent from Table 5 that the maximum stress in the triangular tube is lower than the proof stress at 0.2% from the tensile test. This observation can be explained by the high width to thickness ratio of the triangular tubes (c/t=45) which is higher than the suggested maximum value in BS EN 1993-1-1:2005 (c/t=≤38.7) for Class 1 to 3 cross-sections. The width to thickness ratios of the hollow section with hexagonal and octagonal shapes are 23.8 and 18.3 respectively leading to Class 1-3 cross-sections. The failure modes are summarized in Figure 12. The failure mode of local buckling before yielding of the cross-section was observed for specimen T-H-1 while specimens H-H-1 and O-H-1 failed by inelastic local buckling after the yield stress was reached. It

should be noted that inelastic local buckling appeared at the surface with the welded joint first. This may be attributed by the relative large local imperfection at this surface and also the low ductility of the material. No fracture failure was observed at the welded joint. In Figure 11, it can be seen that there is a distinct drop of the axial load for the axial load-axial shortening curves of specimen T-H-1 which is much earlier than the softening behaviour of specimens H-H-1 and O-H-1. This observation can be explained by the Class 4 classification of specimen T-H-1. The inelastic local buckling was also influenced by the width to thickness ratio. Comparing the softening behaviour of specimen H-H-1 to that of O-H-1, the effect of width to thickness ratio on inelastic local buckling is apparent where the softening behaviour of H-H-1 happened earlier than that in the curve of specimen O-H-1. This observation can be related to the DI values shown in Table 5 where the DI value increases when the cross-section shape changes from hexagonal to octagonal.

The test results for high-strength CFST are summarized in Table 6 where $N_{u,CFST}$ is the load capacity of the specimen and $\delta_{u,CFST}$ is the axial shortening at peak load. The confinement ratio, ξ is defined as $A_s f_y / A_c f_{co}$ where A_s is the cross-sectional area of the steel tube, f_y is the yield stress of the virgin steel plate, A_c is the cross-sectional area of the concrete core and f_{co} is the cylinder strength of the concrete core. The Ductility indices of the CFST are also shown in Table 6. Two types of failure mode were observed for the CFST; one was out-of-plane local buckling (labelled as L) at the middle region of the column, and the other one was elephant's foot buckling (labelled as E) at the column ends. Most of the specimens indicated both two failure modes at the end of the test. The failure mode shown in Table 6 is the first failure mode which occurred after the peak load was reached. Figure 13 shows the failure modes of specimens T-CF-1; H-CF-1 and O-CF-1. Figures 13a and 13b present a clear out-of-plane local buckling failure mode and Figure 13c shows the elephant's foot buckling failure mode at the column end. The enhancement ratios of the load capacity, $N_{u,\,CFST} / N_{u,\,tube,}$ are listed in Table 6. The high strength of the infill concrete can significantly increase the load

capacity and the enhancement ratio is around 3.6, 4.3 and 4.4 for the triangular, hexagonal and octagonal CFST specimens respectively. In Table 6, it is obvious that the axial shortening at peak load is not significantly affected by the changes in cross-section shape, however, the cross-section shape has a substantial influence on the ductility index where the *DI* of triangular CFST is much lower than that of the hexagonal and octagonal specimens. Figure 14 shows the axial load to axial shortening behaviour of specimens with the concrete core. The figure illustrates different softening behaviour for specimens with different cross-section shapes. For specimens T-CF-1 and T-CF-2, it can be seen the load drops rapidly after the peak load whereas the curves of the octagonal and hexagonal specimens decrease at a more moderate slope. An unanticipated finding was the difference in the softening behaviour of the identical specimens O-CF-1 and O-CF-2. This discrepancy could be attributed to the difference of the failure modes where the specimens O-CF-1 failed due to the elephant's foot buckling mode and O-CF-2 failed due to an out-of-plane local buckling mode.

3. Numerical investigation

3.1 Hollow tubes

3.1.1 Constitutive model, element types, boundary conditions and mesh convergence studies

The stress-strain curve generated from the idealized stress-strain curve from coupon test (Figure 7) was used in the finite element (FE) modelling. The average elastic modulus was adopted for the elastic behavior of the steel tubes. The option *PLASTIC model provided by ABAQUS was adopted (Ellobody and Young 2006, Thai et al. 2014) to model the plastic behaviour of the steel. The eigenvalue buckling analysis was conducted to simulate the geometric imperfection using the first buckling mode pattern. Four different imperfection amplitudes were considered: the maximum value of measured imperfection amplitude, 1% of the tube thickness (t/100), 2% of the tube thickness (t/50), and 10% of the tube thickness (t/10). A four-node shell element (i.e. S4R in ABAQUS) was selected for the steel tube (Ellobody and Young 2006, Chan and

Gardner 2008, Tao et al. 2013, Ma et al. 2015). Each end of the column is coupled to a reference point for all degrees of freedom. Loading was applied by imposing axial displacement to the top reference point and the bottom reference point was constrained in all degrees of freedom. Mesh convergence studies were conducted to determine the appropriate mesh configuration which provided convergence of the axial stress-strain curves for the FE models. The optimal mesh size was found by comparing the axial load to axial shortening relationship until the behaviour is identical. The mesh size for stub columns of hollow steel tube is D/20 (Triangle), D/26 (Hexagonal) and D/26 (Octagonal) where *D* is the width of the cross-section as shown in Figure 2.

3.1.2 Validation

The experimental results were used to validate the FE model in this investigation. Table 7 includes the predictions of load capacity, axial shortening at peak load and DI from the FE modelling compared with the experimental results. Figure 15 shows the prediction of axial load to axial shortening behaviour of steel hollow tubes (i.e. T-H-1; H-H-1 and O-H-1). For hollow tubes with triangular section, it was found that the influence of imperfection amplitude is negligible. The FE model based on virgin plate materials matches well with the performance of the welded triangular shape suggesting that the welding effect is minimal for this particular specimen. However, the FE results for the hexagonal and octagonal shapes demonstrate the effect of the cold-forming process and the imperfection amplitude on the structural performance. Figure 15(b) shows that an increase in the imperfection values will reduce the maximum load achieved. Further, it was observed that there is a difference at the region between the yield and the peak loads, which is due to cold-forming enhancement at the bending corners that cannot be captured by the simplified material model used for the current studies. Similar observations and conclusions may be drawn from the results of the octagonal sections in Figure 15(c). It can be seen in Table 7 that, for the specimen H-H-1, the FE model with the largest imperfection amplitude (based on the maximum value obtained from imperfection measurement) underestimates the load capacity ($N_{u,}$

$_{FE}/N_{u,tube}$ =0.84) and overestimates the ductility (DI_{FE}/DI=2.21). Similar observation can be made for the prediction of load capacity and ductility for the octagonal specimens O-H-1 ($N_{u,\,FE}/N_{u,tube}$ =0.88 and DI_{FE}/DI=1.78). The FE model for specimen H-H-1 with an imperfection amplitude of t/100 predicts the ultimate load well while it underestimates the ductility index. For an imperfection amplitude of t/10 the FE model can reasonably predict the ultimate load and the ductility index for specimen O-H-1. In Figure 16, the failure modes for the FE models and the experimental results were compared. It was found the FE models can capture the failure modes of hollow steel tubes very well.

3.2 Concrete-filled tubes

3.2.1 Constitutive models, element types, boundary conditions and mesh convergence studies

In the FE analysis for concrete-filled steel tubes, the constitutive model for steel is identical with that for hollow tubes, and three different constitutive models for concrete obtained from existing literature were compared in the numerical investigation. Imperfection of t/10 was adopted for all the models of CFST.

a. Han et al. (2007)

The confined concrete constitutive model for CFST was firstly proposed by Han et al. (2007) and then extended further in Han (2007). Han (2007) indicates that this model is applicable for the confined concrete with confinement ratios, ξ ranging from 0.2 to 0.5 and for concrete cube strength ranging from 30 to 120 MPa. The derived stress-strain model is as follows:

$$\frac{\sigma}{f_{co}} = \begin{cases} 2(\varepsilon/\varepsilon_o) - (\varepsilon/\varepsilon_o)^2 & for\ (\varepsilon/\varepsilon_o) \le 1 \\ \dfrac{(\varepsilon/\varepsilon_o)}{\left[\beta(\varepsilon/\varepsilon_o - 1)^{\eta} + 1\right]} & for\ (\varepsilon/\varepsilon_o) > 1 \end{cases} \quad (1)$$

where $\varepsilon_o = \varepsilon_{co} + 800\xi^{0.2}10^{-6}$

$\xi = \left(A_s f_y / A_c f_{co}\right)$

For a Circular Section: For a Rectangular Section:

$\eta = 2;$ $\eta = 1.6 + 1.5/(\varepsilon/\varepsilon_o);$

$\beta = \left(2.36\times10^{-5}\right)^{[0.25+(\xi-0.5)^7]}\left(f_{co}\right)^{0.5}\times 0.5$ $\beta = \left(f_{co}\right)^{0.1}/\left(1.2\sqrt{1+\xi}\right)$

where σ is the uniaxial stress of confined concrete, ε is the uniaxial strain of confined concrete, and ε_{co} is the uniaxial strain of unconfined concrete. The stress-strain model for concrete from Han et al. (2007) was used to represent the plastic stress-strain behaviour of the confined concrete core in FE analysis using ABAQUS (6.12), a commercial software package. The Concrete Damaged Plasticity Model (CDPM) provided by ABAQUS was suggested for modelling the behaviour of the confined concrete (Han et al. 2007). The flow potential eccentricity, viscosity, the ratio between biaxial compression and uniaxial compression concrete strength, f_{bo}/f_{co}, the ratio of the second stress invariant on the tensile meridian to that on the compressive meridian, K, and dilation angle ψ are as follows:

Flow potential eccentricity=0.1;

Viscosity=0;

f_{bo}/f_{co}=1.16;

K=0.667; and

Ψ=30.

b. Thai et al. (2014)

Thai et al. (2014) developed a FE model for a high strength steel box column filled with high strength concrete. In this study, the model was validated by a large amount of testing data for the concrete filled steel tubes over a wide range of f_y from 282-779 MPa, for f_{co} from 51 to 164 MPa and width to thickness ratios from 15 to134. There are two portions of this stress-strain model. The initial portion before the peak load adopted the stress-strain model firstly proposed by Popovics (1973) and later modified by Mander (1988):

$$\frac{\sigma}{f_{cc}} = \frac{(\varepsilon / \varepsilon_{cc}) r}{r - 1 + (\varepsilon / \varepsilon_{cc})^{r}}, \quad r = \frac{E_c}{E_c - (f_{cc} / \varepsilon_{cc})} \tag{2}$$

where E_c is the elastic modulus of the concrete; f_{cc} and ε_{cc} are the peak stress and coincident strain of the confined concrete which are adopted from the empirical equations of Xiao et al. (2010).

$$\frac{f_{cc}}{f_{co}} = 1 + 3.24 \left(\frac{f_l}{f_{co}} \right)^{0.8} \tag{3}$$

$$\frac{\varepsilon_{cc}}{\varepsilon_{co}} = 1 + 17.4 \left(\frac{f_l}{f_{co}} \right)^{1.06} \tag{4}$$

where f_l is the confining pressure. Thai et al. (2014) proposed an empirical equation for the confining pressure of high strength concrete in CFST which is as follows:

$$\begin{aligned} f_l &= \frac{(195.118 + 40.611 f_y) e^{-0.1\frac{B}{t}}}{988 - 0.01962 f_{co}} \quad for \frac{B}{t} \le 15 \\ f_l &= \frac{(-42428 + 236 f_y) e^{-0.04\frac{B}{t}}}{7773 + f_{co}^{1.6}} \quad for \frac{B}{t} > 15 \end{aligned} \tag{5}$$

where B is the width of a square cross-section which is taken as equal to the value D shown in Figure 2 in this investigation, and t is the thickness of the steel tube.

For the second portion after the peak load, Thai et al. (2014) adopted an exponential function from Binici (2005).

$$\sigma = f_{re} + (f_{co} - f_{re}) \exp\left[-\left(\frac{\varepsilon - \varepsilon_{cc}}{\alpha} \right)^{0.92} \right] \tag{6}$$

where f_{re} is the residual stress of confined concrete which was taken as 0.1 f_{co}.

$$\alpha = 0.005 + 0.0075\xi \tag{7}$$

Thai et al. (2014) also used the Concrete Damaged Plasticity Model in ABAQUS. The basic parameters in CDPM are shown as follows:

Flow potential eccentricity=0.1;

Viscosity=0;

$f_{bo}/f_{co}=1.5/f_{co}^{0.075}$;

$K=5.5/(5+2f_{co}^{0.075})$; and

$\Psi=40$.

c. *Duarte et al. (2016)*

Duarte et al. (2016) adopted a Eurocode 2 (2004) based concrete model with a proposed linear descending portion after the peak stress. The ascending portion used the suggested stress-strain relationship in Eurocode 2 (BS EN 1992-1-1:2004):

$$\sigma = f_{co}\frac{k\eta - \eta^2}{1+(k-2)\eta} \tag{8}$$

$$\eta = \frac{\varepsilon}{\varepsilon_{co}} \tag{9}$$

$$k = 1.05E_c\frac{\varepsilon_{co}}{f_{co}} \tag{10}$$

For the strain softening portion, Duarte et al. (2016) assumed the stress will degrade linearly as the strain increases. The slope of the descending line E_{c2} is shown as:

$$E_{c2} = \frac{0.1 f_{co}}{0.01 - \varepsilon_{co}} \quad \text{for a circular section}$$
$$E_{c2} = \frac{0.6 f_{co}}{0.01 - \varepsilon_{co}} \quad \text{for a rectangular section} \tag{11}$$

The Concrete Damaged Plasticity Model in ABAQUS was also used in this study. The basic parameters in CDPM are shown as follows:

Flow potential eccentricity=0.1;
Viscosity=0;
f_{bo}/f_{co}=1.16;
K=0.667; and
Ψ=40.

In this numerical investigation, the FE model from Han et al. (2007) is labelled as H-07-C and H-07-R (where C and R indicate circular and rectangular cross-sections respectively), the FE model from Thai et al. (2014) is labelled as T-14, and the FE model from Duarte et al. (2016) is labelled as D-16-C and D-16-R.

For the FE modelling of CFST, a four-node shell element (i.e. S4R in ABAQUS) was selected for the steel tube. An eight-node solid element (i.e. C3D8R in ABAQUS) was used for the concrete core element (Han et al. 2007, Sheehan et al. 2012, Li et al. 2015). The boundary conditions are identical to those of the FE model for hollow steel tubes, with each end of the column is coupled to a reference point in all degrees of freedom. Axial displacement was applied to the top reference point and the bottom reference point was constrained in all degrees of freedom. Mesh convergence studies were conducted. The steel mesh size is identical to the concrete core which is D/6 (Triangle), D/10 (Hexagonal) and D/10 (Octagonal) where D is the width of the cross-section as shown in Figure 2. Surface to surface contact was established between the inner surface of the steel tube and the outer surface of the concrete core. “Hard” contact provided by

ABAQUS which allows for the separation of the two surfaces after contact was selected for normal contact behaviour between the master surface (inner surface of steel tube) and the slave surface (concrete surface). The tangent behaviour between the two surfaces is modelled by the Coulomb friction model with the friction coefficient taken as 0.3.

3.2.2 Validation

The experimental results of the CFST were used to validate the FE model. The FE predictions are shown in Table 7. The averaged test result from two identical specimens was used for this validation. The FE result using the constitutive model of D-16-C was not summarized in Table 7, because a hardening behaviour was observed after the peak load as shown in Figure 17. Figure 17 shows the prediction of axial load to axial shortening behaviour from FE analysis compared with that obtained from tests. It was found that all the constitutive models can provide an accurate prediction of the load capacity of the test specimens with a deviation less than 7%. However, the predictions of axial deformation at peak load are different for the constitutive models. For triangular and hexagonal specimens, the model from Han et al. (2007) for rectangular sections CFST (H-07-R) achieved the best prediction for $\delta_{u,CFST}$. For specimens with octagonal cross-section the model of H-07-C can predict the value of $\delta_{u,CFST}$ well. The concrete models of T-14 and D-16-R underestimate the deformation at peak load. In the case of the ductility index, all the concrete models cannot provide an accurate prediction of *DI* for the triangular specimens. The concrete model from Han et al. (2007) (H-07-R) provides the best prediction of *DI* for the hexagonal specimens (DI_{FE}/DI=0.95*)*. For the specimens with octagonal cross-section, models of H-07-R, T-14, and D-16-R provided reasonable prediction of the *DI* value with ratios of DI_{FE}/DI ranging from 0.93 to 1.1. Similar observations can be made for Figure 17, where the softening behavior of triangular specimens cannot be captured as shown in Figure 17 (a). Only the model of H-07-R can provide a good prediction of the softening behaviour of hexagonal specimens. For specimens with octagonal cross-section, the models of H-07-R, T-14,

and D-16-R capture the softening behaviour. Figure 16 shows the predictions of failure mode from the FE models for the concrete model of H-07-R.

4. Assessment on Design Approaches

4.1 Eurocode 4 (BS EN 1994-1-1:2004)

Eurocode 4 (BS EN 1994-1-1:2004) provides two formulae for the load capacity of CFST. One is a general formula where the cross-section shape of CFST is not specified. The other one is for CFSTs with a circular cross-section which considers the effect of confinement. These two formulae are shown as follows. Measured yield strength f_y and measured compressive cylinder strength f_{co} are used in this assessment.

$$N = A_s f_y + A_c f_{co} \quad \text{for general section} \tag{12}$$

$$N = \eta_a A_s f_y + A_c f_{co}\left(1+\eta_c \frac{t}{d}\frac{f_y}{f_{co}}\right) \quad \text{for circular section} \tag{13}$$

In the case of uniaxial load:

$$\eta_a = 0.25\left(3+2\bar{\lambda}\right) \le 1 \tag{14}$$

$$\eta_c = 4.9 - 18.5\bar{\lambda} + 17\bar{\lambda}^2 \ge 0$$

$$\bar{\lambda} = \sqrt{\frac{N}{N_{cr}}} \tag{15}$$

where N_{cr} is the elastic critical force.

4.2 American code (ACI 318-11/AISC 360-16)

American code (ACI 318-11/AISC 360-16) provides a simple formulae for CFST. It is suggested the load capacity of CFST is given as the sum of the load capacity of the steel and concrete components. The beneficial effect of confinement for circular CFST is also considered. The design formulae are shown as follows. Similarly, measured yield

strength f_y and measured compressive cylinder strength f_{co} are used in this assessment:

$$N = A_s f_y + 0.85 A_c f_{co} \qquad \text{for general section} \tag{16}$$

$$N = A_s f_y + 0.95 A_c f_{co} \qquad \text{for circular section} \tag{17}$$

4.3 Chinese code (GB50936-2014)

Chinese code (GB50936-2014) provides a specified formulae for CFST with an octagonal cross-section which considers the effect of confinement. Chinese code (GB50936-2014) also covers the cross-section shapes of circular, square (rectangular) and hexadecagonal. Circular and hexadecagonal sections share the same design equation and rectangular sections should be converged to an equivalent square section. Only the design formulae for octagonal sections were presented and assessed in this paper. The design formula is summarised as follows. For consistency, measured yield strength f_y and measured compressive cube strength $f_{co,cube}$ are used in this assessment:

$$N = A_{sc} f_{sc} \tag{18}$$

$$f_{sc} = \left(1.212 + B\xi + C\xi^2\right) 0.63 f_{co,cube} \tag{19}$$

$$B = 0.140 f_y / 213 + 0.778 \tag{20}$$

$$C = -0.07(0.63 f_{co,cube})/14.4 + 0.026 \tag{21}$$

where ξ is the confinement ratio, A_{sc} is the cross-section area of CFST which is the total cross-section area of the steel tube and the concrete core; f_{sc} is the equivalent strength of a CFST, $f_{co,cube}$ is the cube strength of concrete.

4.4 Assessment

The existing design codes do not consider CFST with triangular and hexagonal cross-section shapes. The Chinese code only considers an octagonal cross-section. The load capacity according to the different code provisions is assessed and compared to the experimental results. The equivalent diameter D_{eq} was used in the design formulae for circular CFST.

$$D_{eq} = \frac{P}{2\pi} \tag{22}$$

where P is the perimeter of the original cross-section.

The assessment is summarized in Table 8. The general design approach from Eurocode 4, Eq. (12), provided the best predictions of the test results. The ratio between the calculated values and the test results (N_d/N_u) is around 0.99. The design approach in Eurocode 4 (BS EN 1994-1-1:2004) for circular CFST overestimate the load capacity of the test specimens (by up to 4%). This is believed to be attributable to the lower levels of confinement provided by triangular, hexagonal and octagonal CFST cross-sections compared to circular CFST. The design approach of ACI 318-11/AISC 360-16 provide a more conservative prediction with a ratio of N_d/N_u around 0.88 for general cross-sections. The Chinese code (GB50936-2014) for octagonal CFST provides a less conservative prediction with a 10 % underestimation of axial load capacity.

5. Conclusions

This paper has presented an experimental investigation for hollow steel tubes and steel tubes filled with high strength concrete with triangular, hexagonal and octagonal cross-sections under uniaxial compression. The concrete compressive cylinder strength was around 100 MPa. Finite element models incorporating three existing concrete constitutive models were also developed and compared to the experimental results. Existing design approaches for CFST were also assessed. The following conclusions

may be made based on the experimental and numerical studies described in this paper:

(1) For concrete filled steel tubes, the in-filled high strength concrete can significantly enhance the load capacity of steel tube. The enhancement ratio of load capacity (concrete filled vs. hollow tube) found in the experimental investigation is up to 4.5 for octagonal CFST. It is also found that the cross-sectional shape affects the ductility and the softening behaviour of the CFST.

(2) In the finite element analysis, the behaviour of hollow steel tube under axial compression can be predicted reasonably well. The existing concrete constitutive models provide good predictions of the load capacity of CFST. However, the three concrete models cannot accurately capture the softening behaviour of triangular specimens. The concrete model of H-07-R from Han et al. (2007) can capture the behaviour of hexagonal and octagonal CFST reasonably.

(3) In assessing the design approaches, it is found that the approach using the general design formulae from Eurocode 4 (BS EN 1994-1-1:2004) can provide an accurate prediction of the axial load capacity for CFST cross-sections considered in this investigation with a deviation of 1%. The design approach from ACI 318-11/AISC 360-16 provide a more conservative prediction (up to 13%). The Chinese code (GB50936-2014) for octagonal CFST provides a less conservative prediction with 9 % underestimation of the axial load capacity.

6. ACKNOWLEDGEMENT

Authors are thankful for the seed funds from the Hong Kong Polytechnic University. This publication was also partly supported by the research funding from the Construction Industry Council under the project “Application of Polygonal High Strength Concrete-filled Composite Column in Seismic-resistant Buildings in Hong Kong”. The support on the experimental works from Mr Ka-Leung CHUNG, Mr Lee Fui-Mau LEE and Miss Mei-Yee LI is also gratefully acknowledged.

Reference

ABAQUS (2012). *ABAQUS Analysis User's Manual*, version 6.12.

ACI (2011) ACI 318-11: Building Code Requirements for Structural Concrete (ACI 318-11) and Commentary. American Concrete Institute, Farmington Hills, MI, USA.

AISC (2016), ANSI/AISC 360-16: Specification for Structural Steel Buildings, American Institute of Steel Construction, Chicago, IL.

Binici, B. (2005) An analytical model for stress–strain behavior of confined concrete. *Engineering structures*, **27(7)**: 1040-1051.

BSI (2004) BS EN 1992-1-1:2004: Eurocode 2 Design of concrete structures, Part 1.1, General rules and rules for buildings. BSI, London, UK

BSI (2004) BS EN 1994-1-1:2004: Eurocode 4 Design of steel and concrete structures, Part 1.1, General rules and rules for buildings. BSI, London, UK

BSI (2005) BS EN 1993-1-1:2005: Eurocode 3 Design of steel structures, Part 1.1, General rules and rules for buildings. BSI, London, UK

BSI (2009) BS EN ISO 6892-1: Metallic materials: Tensile testing, Part 1: Method of testing at ambient temperature. BSI, London, UK.

BSI, (2009) BS EN 12390-3: Testing harden concrete: Compressive strength of test specimens. BSI, London, UK.

Chan, T.M. and Gardner, L. (2008) Compressive resistance of hot-rolled elliptical hollow sections. *Engineering Structures* **30(2)**: 522–532.

Chan, T.-M., Huai, Y.-M and Wang, W. (2015) Experimental investigation on lightweight concrete-filled cold-formed elliptical hollow section stub columns. *Journal of Constructional Steel Research* **115**, 434-444.

China Architecture and Building Press (2004) GB50936-2014: Technical code for concrete filled steel tubular structure. China Architecture and Building Press, Beijing, China (in Chinese).

Duarte, A.P.C., Silva, B.A., Silvestre, N., de Brito, J., Júlio, E. and Castro, J.M. (2016) Finite element modelling of short steel tubes filled with rubberized concrete. *Composite Structures*, **150**: 28-40.

Ellobody, E. and Young, B. (2006) Nonlinear analysis of concrete-filled steel SHS and

RHS columns. *Thin-walled structures* **44(8)**: 919-930.

Evirgen, B., Tuncan, A. and Taskin, K. (2014) Structural behavior of concrete filled steel tubular sections (CFT/CFSt) under axial compression. *Thin-Walled Structures*, **80**: 46-56.

Furlong, R.W. (1967) Strength of steel-encased concrete beam columns. *Journal of the Structural Division, American Society of Civil Engineers* **93**: 113.

Giakoumelis, G. and Lam, D. (2004) Axial capacity of circular concrete-filled tube columns. *Journal of Constructional Steel Research* **60(7)**: 1049-1068.

Han, L.H. (2002) Tests on stub columns of concrete-filled RHS sections. *Journal of Constructional Steel Research*, **58(3)**: 353-372.

Han, L.H., Yao, G.H. and Tao, Z. (2007) Performance of concrete-filled thin-walled steel tubes under pure torsion. *Thin-Walled Structures*, **45(1)**: 24-36.

Han. L.H. (2007) *Concrete-filled steel tubular structures-theory and practice.* Science Press, Beijing, China [in Chinese].

Huang, Y. and Young, B. (2014) The art of coupon tests. *Journal of Constructional Steel Research* **96**: 159-175.

Kloppel, V.K. and Goder, W. (1957) An investigation of the load carrying capacity of concrete-filled steel tubes and development of design formula. *Der Stahlbau*, **26(2)**:44-50.

Li, W., Han, L.-H. and Chan, T.-M. (2015) Performance of concrete-filled steel tubes subjected to eccentric tension. *Journal of Structural Engineering*, 10.1061/(ASCE)ST.1943-541X.0001304, 141(12), 04015049-1 to 04015049-9, ASCE.

Liew JYR and Xiong DX. (2010) Experimental investigation on tubular columns infilled with ultra-high strength concrete. In *Proceedings of the 13th International Symposium on Tubular Structures.* Hong Kong, China, 2010, 637–645.

Liu. X and Chung K. F. (2016) Experimental investigation into residual stresses of welded H-sections made of Q690 steel materials, In *Proceeding of the Fourteenth East Asia-Pacific Conference*. Ho Chi Minh City, p559-566.

Ma, J.-L, Chan, T.-M. and Young, B. (2015) Experimental investigation on stub-column behavior of cold-formed high-strength steel tubular sections. *Journal of Structural*

Engineering, 10.1061/(ASCE)ST.1943-541X.0001456, 04015174-1 to 04015174-11. ASCE.

Mander, J.B., Priestley, M.J. and Park, R. (1988) Theoretical stress-strain model for confined concrete. *Journal of structural engineering*, **114(8)**: 1804-1826.

O'Shea, M.D. and Bridge, R.Q. (2000) Design of circular thin-walled concrete filled steel tubes. *Journal of Structural Engineering* **126(11)**: 1295-1303.

Popovics, S. (1973) A numerical approach to the complete stress-strain curve of concrete. *Cement and concrete research*, **3(5)**: 583-599.

Ren, Q.X., Han, L.H., Lam, D. and Hou, C. (2014) Experiments on special-shaped CFST stub columns under axial compression. *Journal of Constructional Steel Research* **98**: 123-133.

Sheehan, T., Dai, X.H., Chan, T.M. and Lam, D. (2012) Structural response of concrete-filled elliptical steel hollow sections under eccentric compression. *Engineering Structures* **45**, 314–323.

Schneider, S.P. (1998) Axially loaded concrete-filled steel tubes. *Journal of structural Engineering* **124(10)**: 1125-1138.

Susantha, K.A.S., Ge, H. and Usami, T. (2001) Uniaxial stress–strain relationship of concrete confined by various shaped steel tubes. *Engineering Structures* **23(10)**: 1331-1347.

Tao, Z., Han, L.H. and Zhao, X.L. (1998) Behaviour of square concrete filled steel tubes subjected to axial compression. In *Proceedings of the fifth international conference on structural engineering for young experts.* Shenyang, PR China, pp. 61-67.

Tao, Z., Wang, Z.B. and Yu, Q. (2013) Finite element modelling of concrete-filled steel stub columns under axial compression. *Journal of Constructional Steel Research* **89**: 121-131.

Thai, H.T., Uy, B., Khan, M., Tao, Z. and Mashiri, F. (2014) Numerical modelling of concrete-filled steel box columns incorporating high strength materials. *Journal of Constructional Steel Research* **102**: 256-265.

Tomii, M., Yoshimura, K. and Morishita, Y. (1977) Experimental studies on concrete-filled steel tubular stub columns under concentric loading. In *Stability of Structures Under Static and Dynamic Loads* 1977, SSRC/ASCE, Washington, pp.718-741.

Xiao, Q.G., Teng, J.G. and Yu, T. (2010) Behavior and modeling of confined high-

strength concrete. *Journal of Composites for Construction*, **14(3)**: 249-259.

Xu, W., Han, L.H. and Li, W. (2016) Performance of hexagonal CFST members under axial compression and bending. *Journal of Constructional Steel Research*, **123:** 162-175.

Yu, M., Zha, X., Ye, J. and Li, Y. (2013) A unified formulation for circle and polygon concrete-filled steel tube columns under axial compression. *Engineering structures* **49**: 1-10.

Table captions

Figure captions

Table 1 Dimensions and imperfections of specimens

	Width, *D* mm	**Thickness, *t* mm**	***D/t***	**Height mm**	**Maximum local imperfection, *ω* mm**	***ω/t***
T-H-1	126.9	3.0	42	449.5	0.53	0.18
T-CF-1	125.8	3.0	42	448.5	0.53	0.18
T-CF-2	125.8	3.0	42	451.0	0.38	0.13
H-H-1	157.2	3.1	51	448.5	0.63	0.19
H-CF-1	156.9	2.9	54	451.0	0.47	0.16
H-CF-2	157.6	2.9	54	450.5	0.57	0.21
O-H-1	155.7	3.1	50	449.0	0.89	0.30
O-CF-1	155.3	2.9	54	448.5	0.76	0.25
O-CF-2	155.4	2.9	54	450.5	0.89	0.30

Table 2 Test results of tensile coupon tests

	E_s **MPa**	$\sigma_{0.2\text{-t}}$ **MPa**	σ_u **MPa**	ε_f
Coupon 1	189000	285	463	28%
Coupon 2	199000	301	467	29%
Coupon 3	195000	303	452	26%
Average	194000	296.3	460.7	27.7%

Table 3 Mix proportions of concrete

Content	**Proposed Quantity**	**Mass for *casting***
Water	128 kg/m^3	9.4 kg
Cement	512 kg/m^3	44.8 kg
Sand	717 kg/m^3	64.3 kg
10 mm Aggregate	430 kg/m^3	37.7 kg
20 mm Aggregate	645 kg/m^3	56.6 kg
Superplasticizer	15 kg/m^3	1.30 kg

Table 4 Concrete material tests

Type	**Specimen**	**Strength**	**Mean strength**	**Elasticity E_c**	**Mean E_c**
		MPa	MPa	GPa	GPa
Cube	Cube 1	111.0	109.5	N/A	N/A
	Cube 2	109.9			
	Cube 3	111.7			
	Cube 4	106.5			
	Cube 5	108.2			
Cylinder	Cylinder 1	95.3	N/A	40.7	N/A
	Cylinder 2	87.7		41.5	
	Cylinder 3	101.0	100.3	41.6	41.5
	Cylinder 4	100.6		42.8	
	Cylinder 5	99.1		40.1	

Table 5 Test results of hollow steel tubes

Specimens	$N_{u,tube}$ **kN**	$\delta_{u,tube}$ **mm**	***DI***	$\sigma_{0.2}$ **MPa**	$\sigma_{0.2}/\sigma_{0.2\text{-}t}$	**Failure mode**
T-H-1	325	0.73	1.41	258.0	0.88	Local buckling
H-H-1	438	2.57	1.59	309.8	1.06	Yield
O-H-1	449	3.88	1.83	304.6	1.04	Yield

Table 6 Test results of concrete filled steel tubes

Specimens	$N_{u,CFST}$ **kN**	$\delta_{u,CFST}$ **mm**	ξ	$N_{u,CFST}/N_{u,tube}$	***DI***	**Failure mode**
T-CF-1	1145	1.47	0.47	3.5	1.11	L
T-CF-2	1210	1.67	0.47	3.7	1.10	L
H-CF-1	1912	1.67	0.28	4.4	1.46	L
H-CF-2	1866	1.67	0.28	4.3	1.44	L
O-CF-1	1970	1.71	0.26	4.4	1.90	E
O-CF-2	2024	1.87	0.26	4.5	1.41	L

Table 7 FE results of hollow steel tubes and CFSTs

Specimens	**Imperfection mm**	$N_{u,FE}$ **kN**	$N_{u,FE}/N_{u,tube}$	$\delta_{u,FE}$ **mm**	$\delta_{u,FE}/\delta_{u,tube}$	DI_{FE}	DI_{FE}/DI
T-H-1	0.03 (t/100)	339	1.04	0.68	0.93	1.28	0.91
	0.06 (t/50)	337	1.04	0.67	0.92	1.29	0.91
	0.3 (t/10)	320	0.98	0.65	0.89	1.38	0.98
	0.53 (max.)	307	0.94	0.65	0.89	1.47	1.04
H-H-1	0.03 (t/100)	434	0.99	4.16	1.62	1.18	0.74
	0.06 (t/50)	417	0.95	3.18	1.24	1.29	0.81
	0.3 (t/10)	385	0.88	1.49	0.58	1.87	1.18
	0.63 (max.)	368	0.84	0.74	0.29	3.52	2.21
O-H-1	0.03 (t/100)	477	1.06	6.77	1.74	1.41	0.77
	0.06 (t/50)	477	1.06	6.77	1.74	1.41	0.77
	0.3 (t/10)	441	0.98	4.32	1.11	1.97	1.08
	0.89 (max.)	394	0.88	2.17	0.56	3.26	1.78
Specimens	**Concrete model (Imperfection)**	$N_{u,FE}$ **kN**	$N_{u,FE}/N_{u,CFST}$	$\delta_{u,FE}$ **mm**	$\delta_{u,FE}/\delta_{u,CFST}$	DI_{FE}	DI_{FE}/DI
T-CF-1 T-CF-2	H-07-C (t/10)	1143	0.97	1.72	1.10	2.16	1.95
	H-07-R (t/10)	1125	0.96	1.52	0.97	1.28	1.16
	T-14 (t/10)	1120	0.95	1.25	0.80	1.56	1.41
	D-16-R (t/10)	1097	0.93	1.25	0.80	1.48	1.34
H-CF-1 H-CF-2	H-07-C (t/10)	1886	1.00	1.94	1.16	3.37	2.32
	H-07-R (t/10)	1840	0.97	1.57	0.94	1.38	0.95
	T-14 (t/10)	1847	0.98	1.12	0.67	1.89	1.30
	D-16-R (t/10)	1815	0.96	1.20	0.72	1.92	1.32

O-CF-1 O-CF-2	H-07-C (t/10)	2042	1.02	1.99	1.11	3.87	2.34
	H-07-R (t/10)	2000	1.00	1.48	0.83	1.54	0.93
	T-14 (t/10)	2017	1.01	1.20	0.67	1.82	1.10
	D-16-R (t/10)	1966	0.98	1.29	0.72	1.70	1.03

Table 8 Design assessment

Specimens	**BS EN 1994-1-1**				**ACI 318-11/AISC 360-05**				**GB50936-2014**	
	General		**Circular**		**General**		**Circular**		**Octagonal**	
	N_d	N_d/N_u	N_d	N_d/N_u	N_d	N_d/N_u	N_d	N_d/N_u	N_d	N_d/N_u
T-CF-1	1159	1.01	1242	1.08	1041	0.91	1120	0.98	1090	0.95
T-CF-2	1159	0.96	1242	1.03	1041	0.86	1120	0.93	1090	0.90
Mean		***0.99***		***1.06***		***0.89***		***0.95***		***0.93***
H-CF-1	1878	0.98	2047	1.07	1657	0.87	1804	0.94	1718	0.90
H-CF-2	1878	1.01	2047	1.10	1657	0.89	1804	0.97	1718	0.92
Mean		***0.99***		***1.08***		***0.88***		***0.96***		***0.91***
O-CF-1	1980	1.01	2163	1.10	1744	0.89	1901	0.97	1808	0.92
O-CF-2	1980	0.98	2163	1.07	1744	0.86	1901	0.94	1808	0.89
Mean		***0.99***		***1.08***		***0.87***		***0.95***		***0.91***

Unit kN.

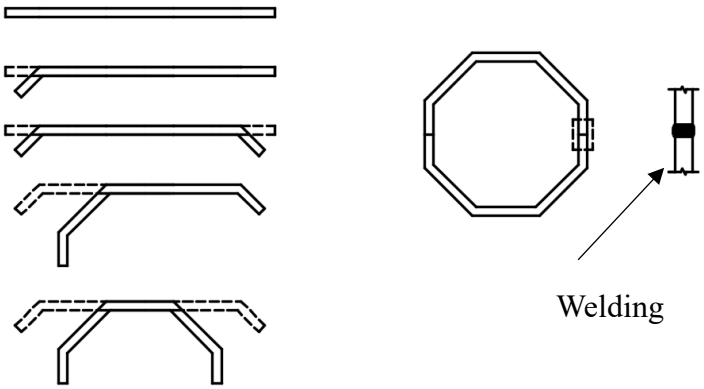

(a) Octagonal

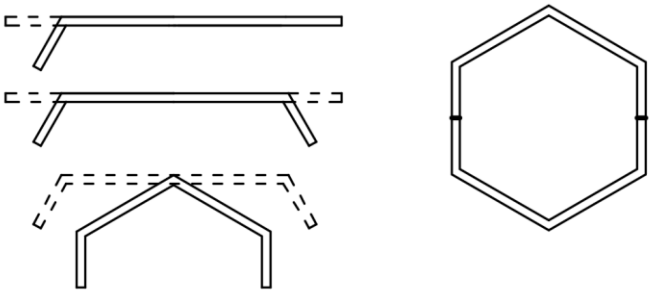

(b) Hexagonal

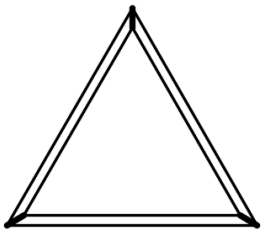

(c) Triangular

Figure 1. Fabrication of steel tubes

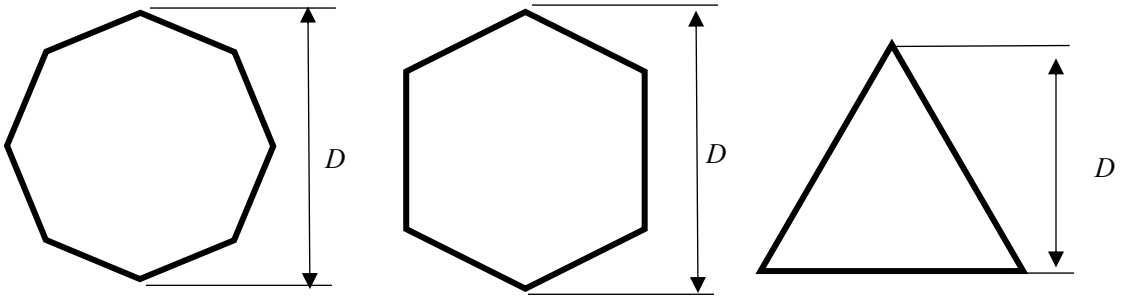

(a) Octagonal (b) Hexagonal (c) Triangular

Figure 2. Width *D* for each cross-section

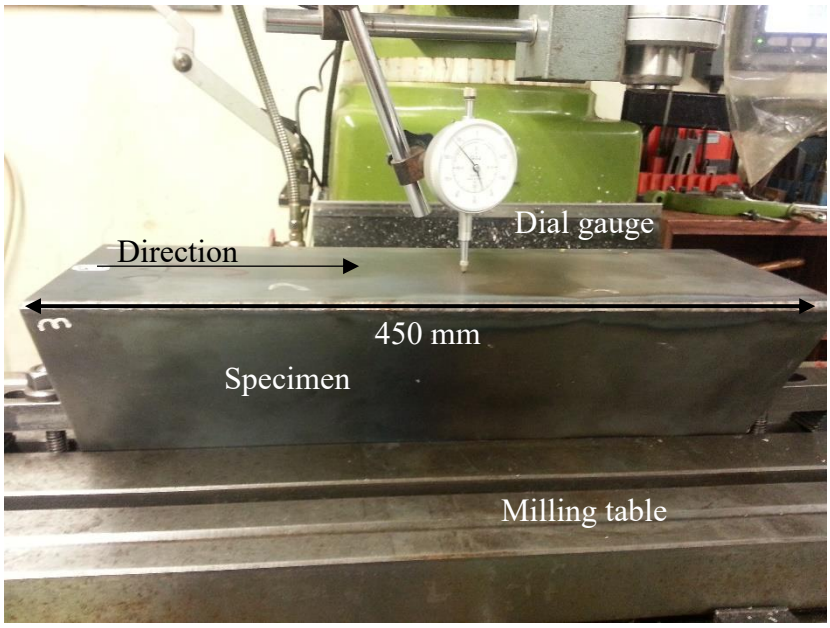

Figure 3. Imperfection measurement

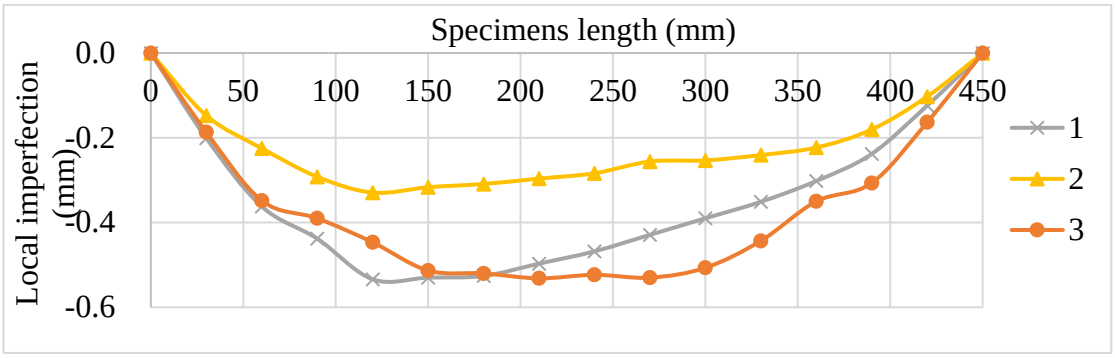

(a) T-H-1

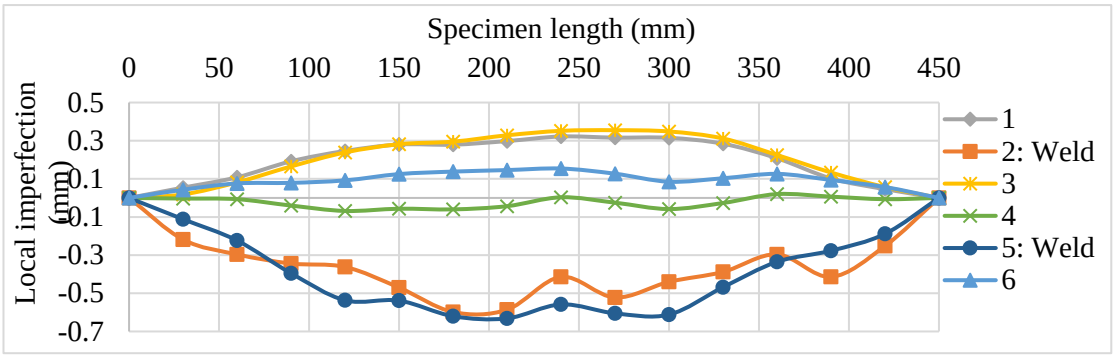

(b) H-H-1

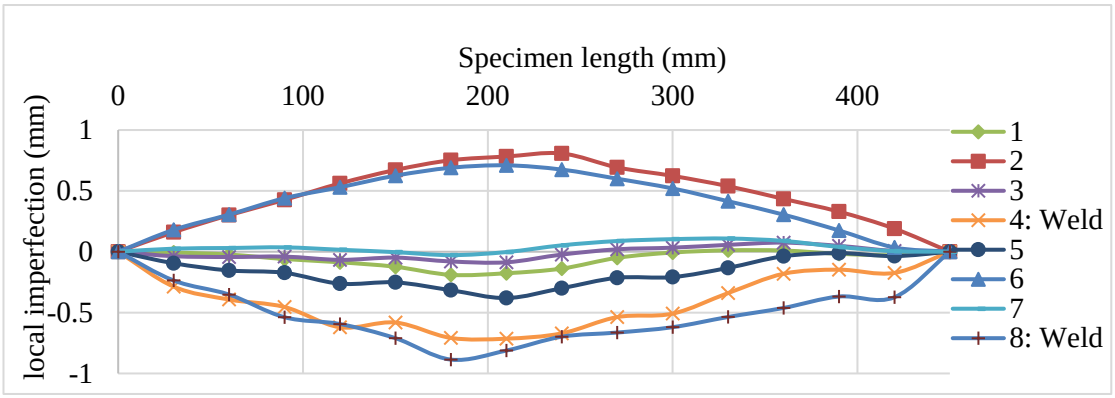

(c) O-H-1

Figure 4. Imperfection profiles

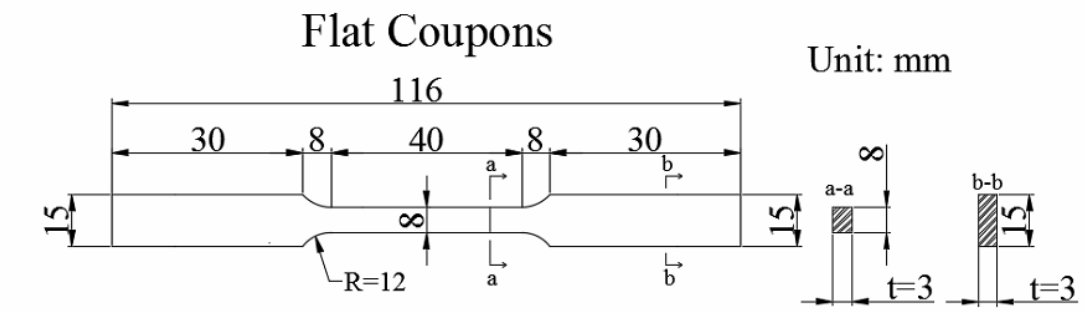

Figure 5. Dimensions of tensile coupon

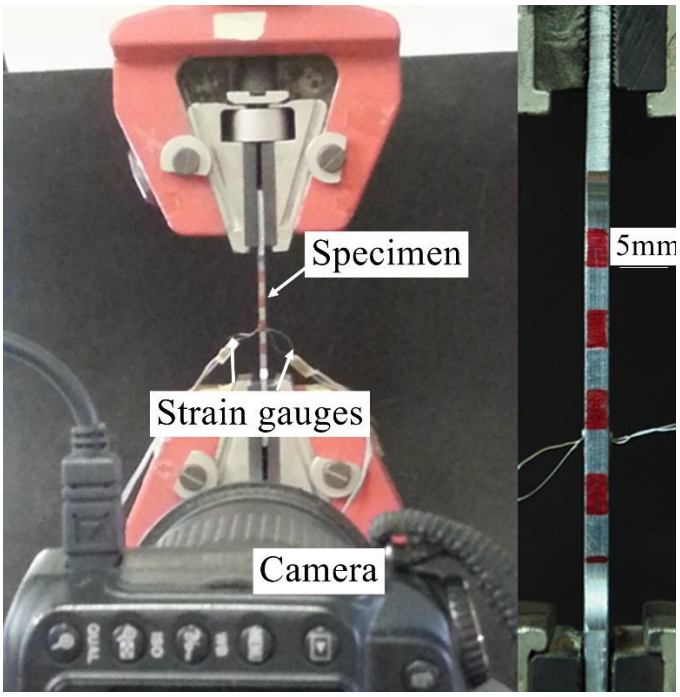

Figure 6. Set up of tensile coupon test

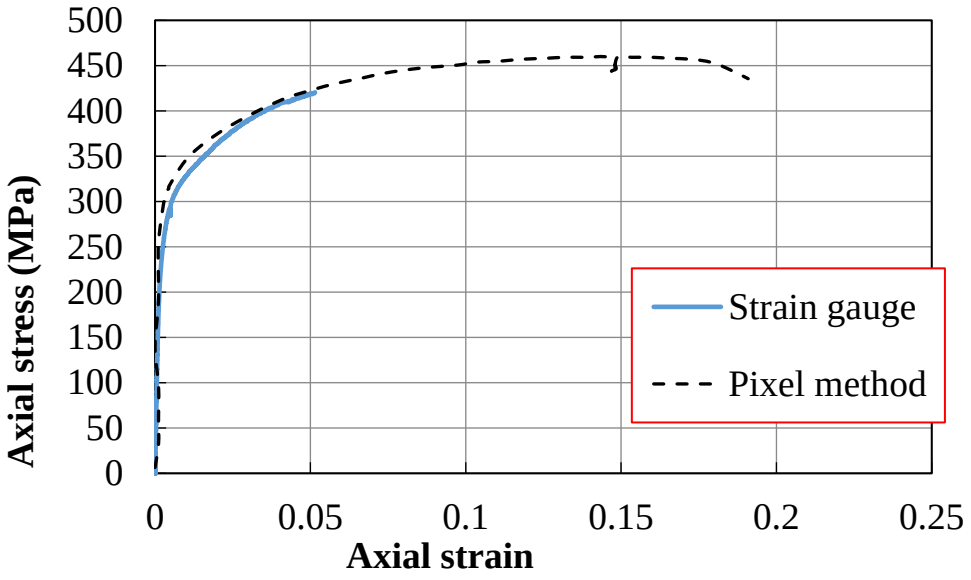

(a) Stress-strain curves from strain gauge and pixel method

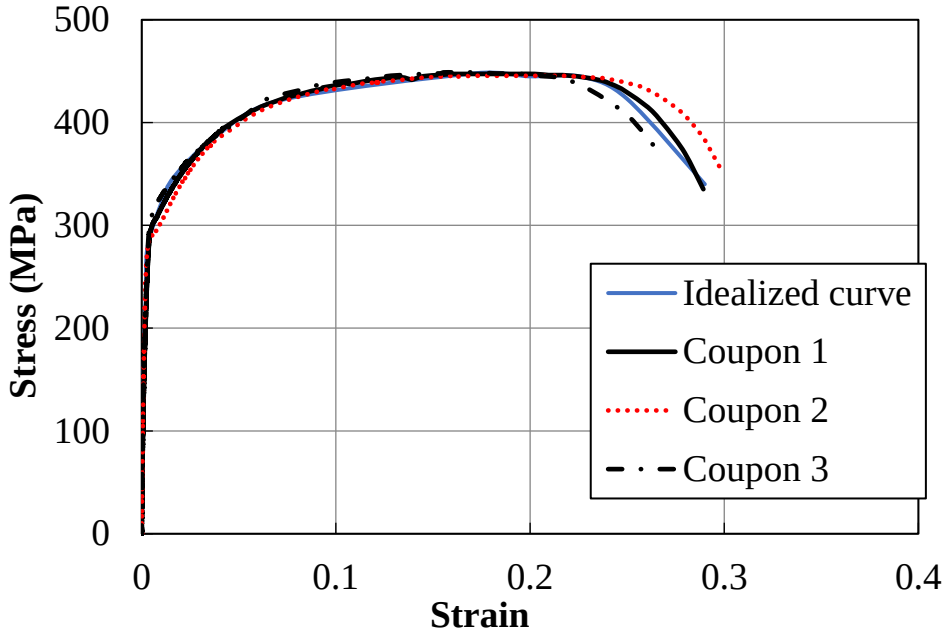

(b) Static stress-strain curves

Figure 7. Stress-strain curves of the tensile coupons

Figure 8. Curing of concrete cylinders and cubes

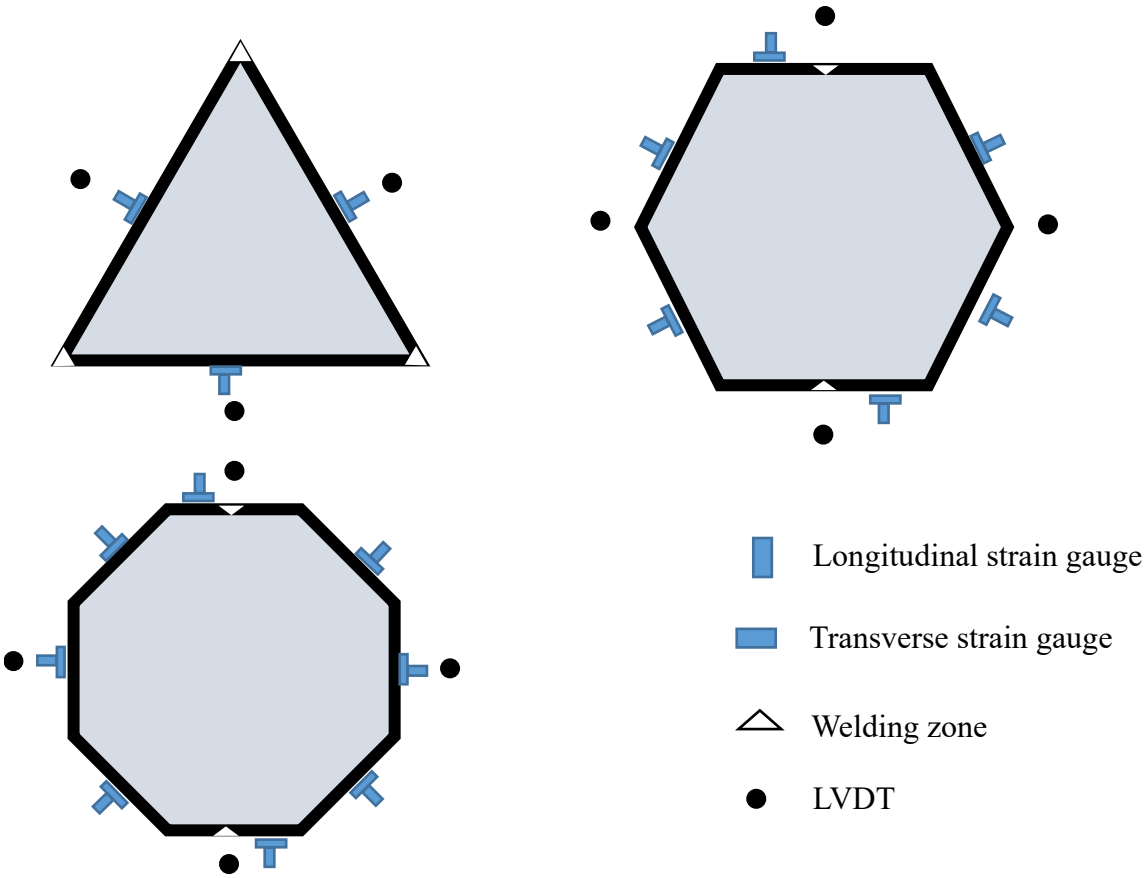

Figure 9. Arrangement of LVDTs and strain gauges

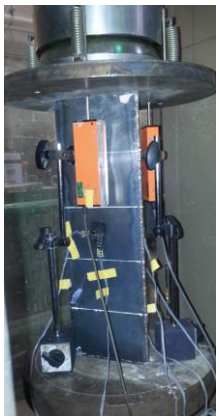

(a) Triangular

(b) Hexagonal

(c) Octagonal

Figure 10. Test set up

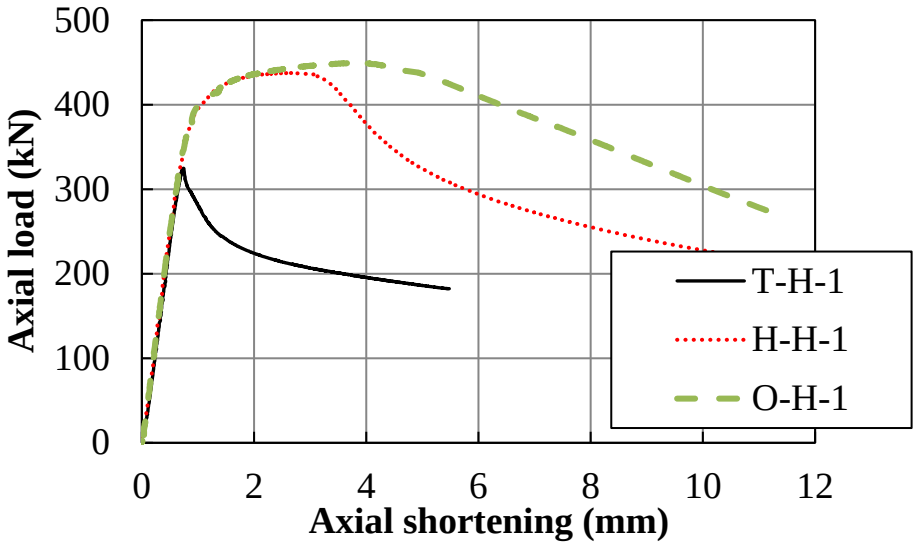

Figure 11. Axial load to axial shortening behavior of hollow steel tubes

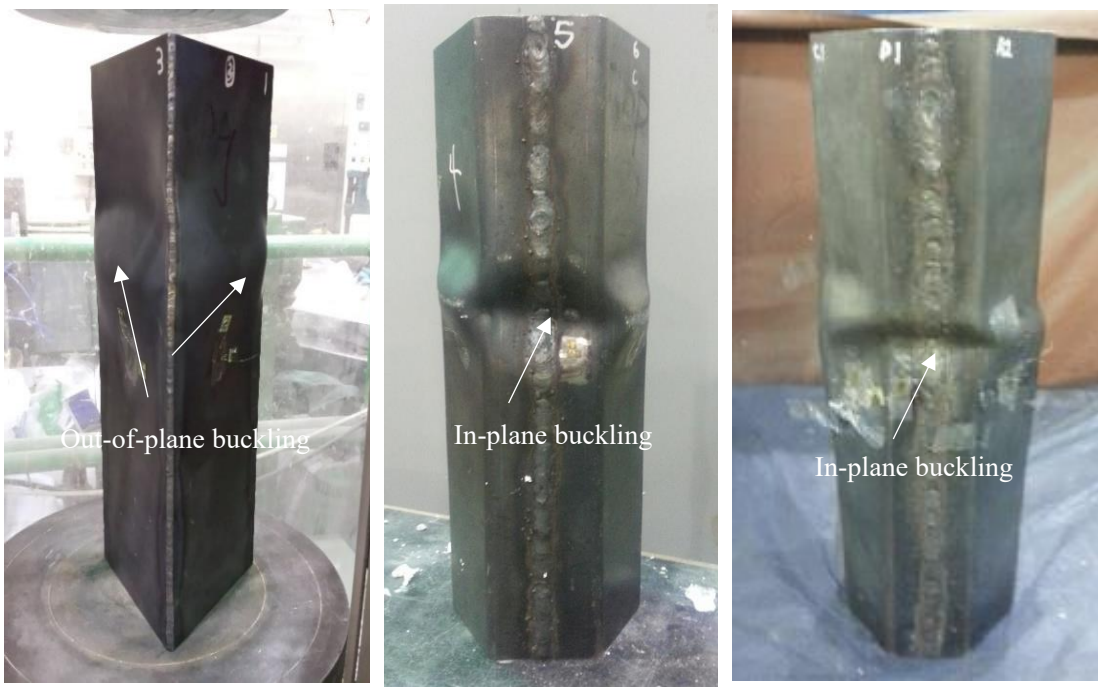

(a) T-H-1 (b) H-H-1 (c) O-H-1

Figure 12. Failure modes of hollow steel tubes

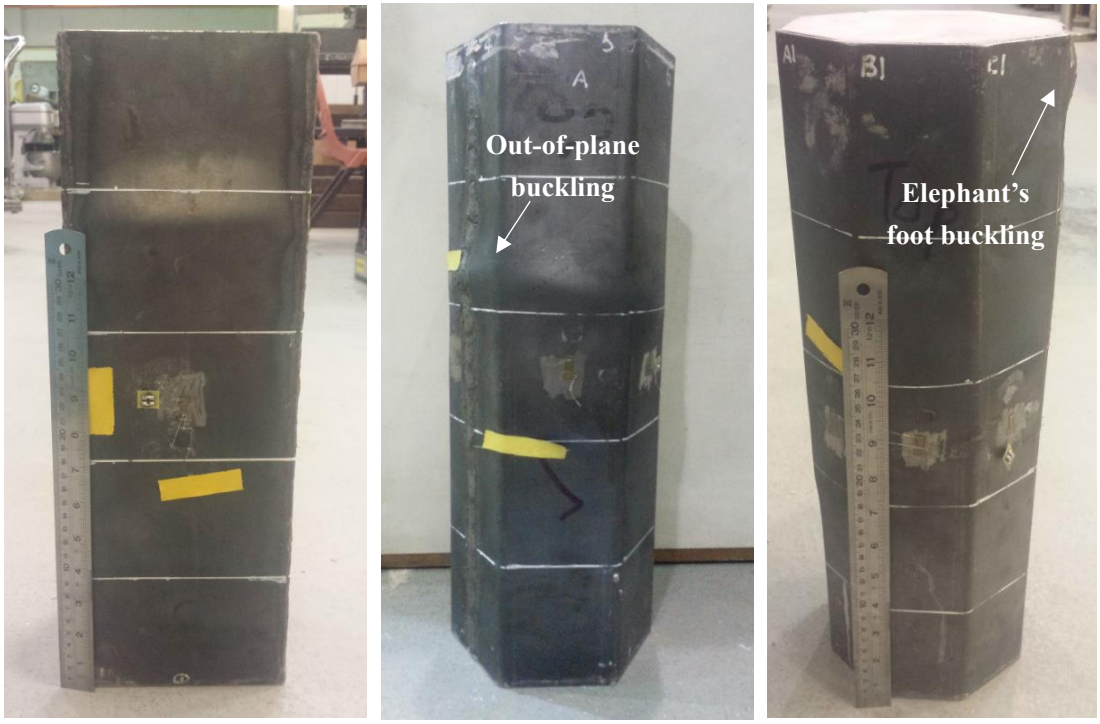

(a) T-CF-1 (b) H-CF-1 (c) O-CF-1

Figure 13 Failure modes of CFSTs

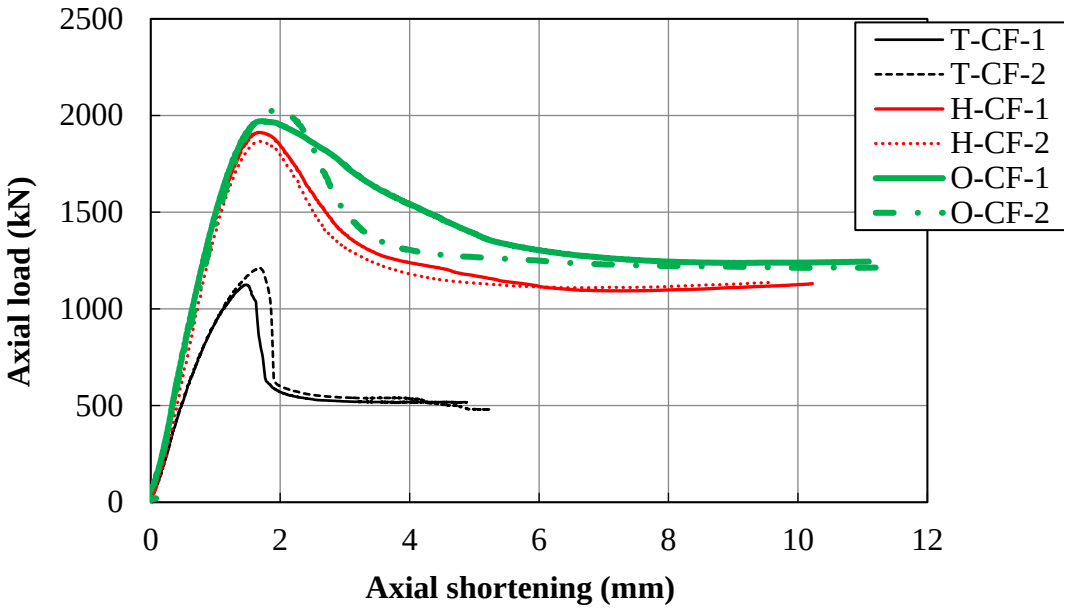

Figure 14. Axial load to axial shortening behavior of CFSTs

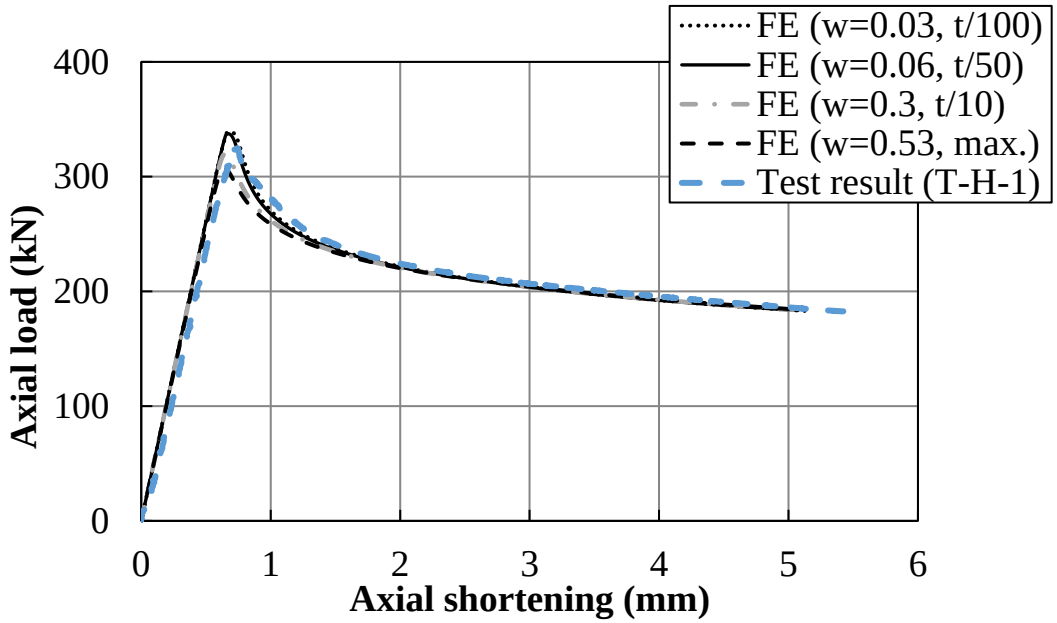

(a) Triangular

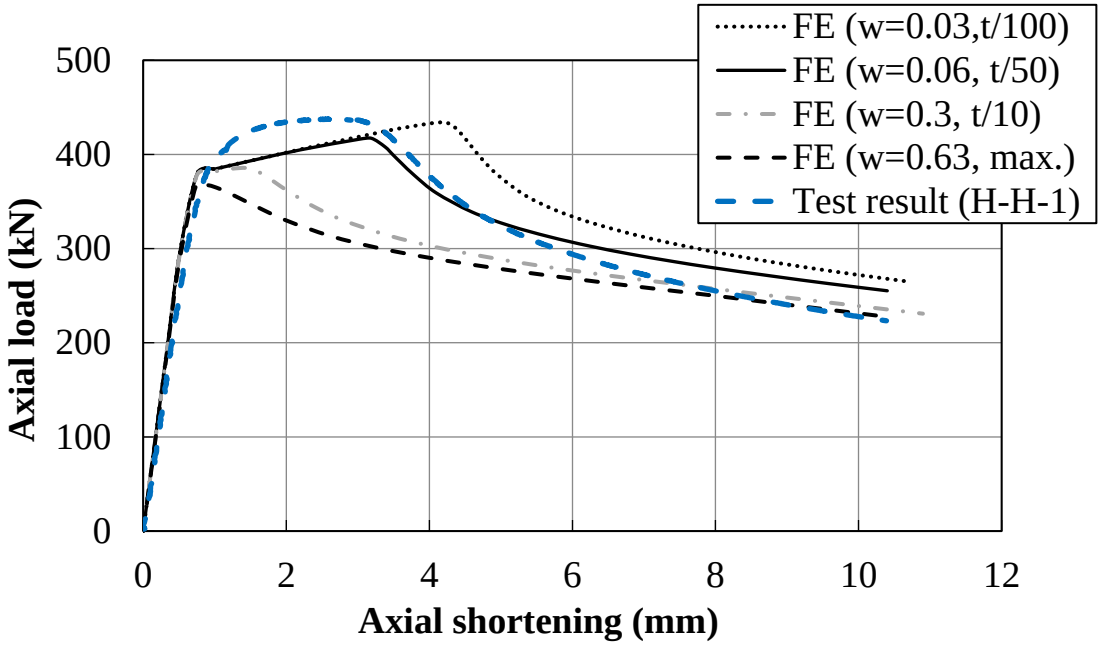

(b) Hexagonal

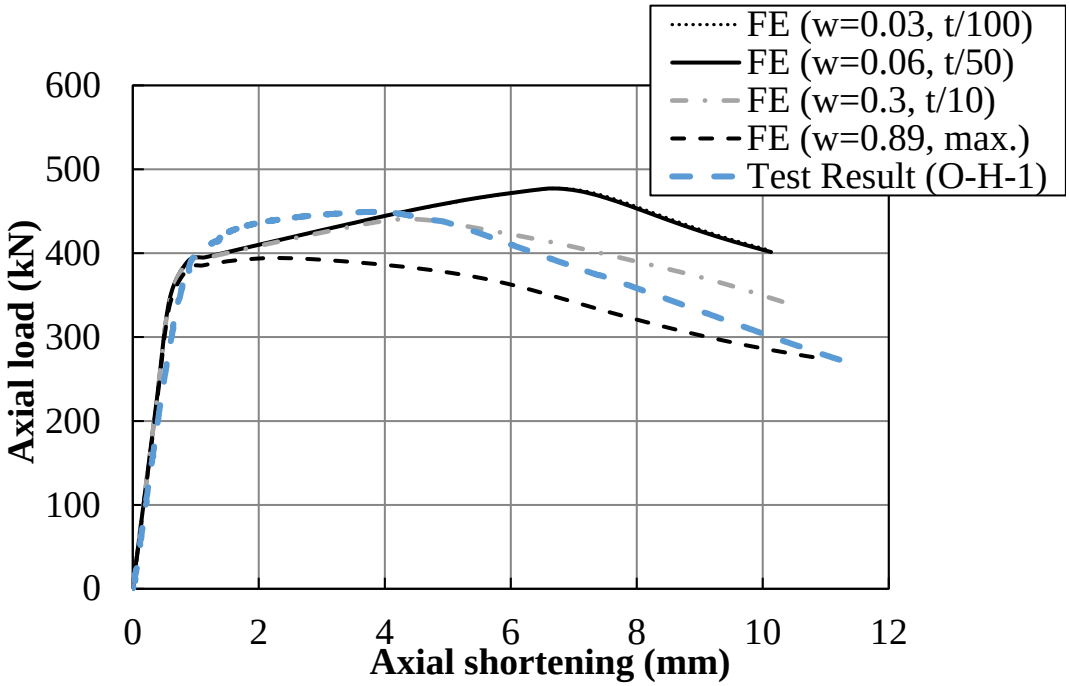

(c) Octagonal

Figure 15. FE predictions for hollow steel tubes

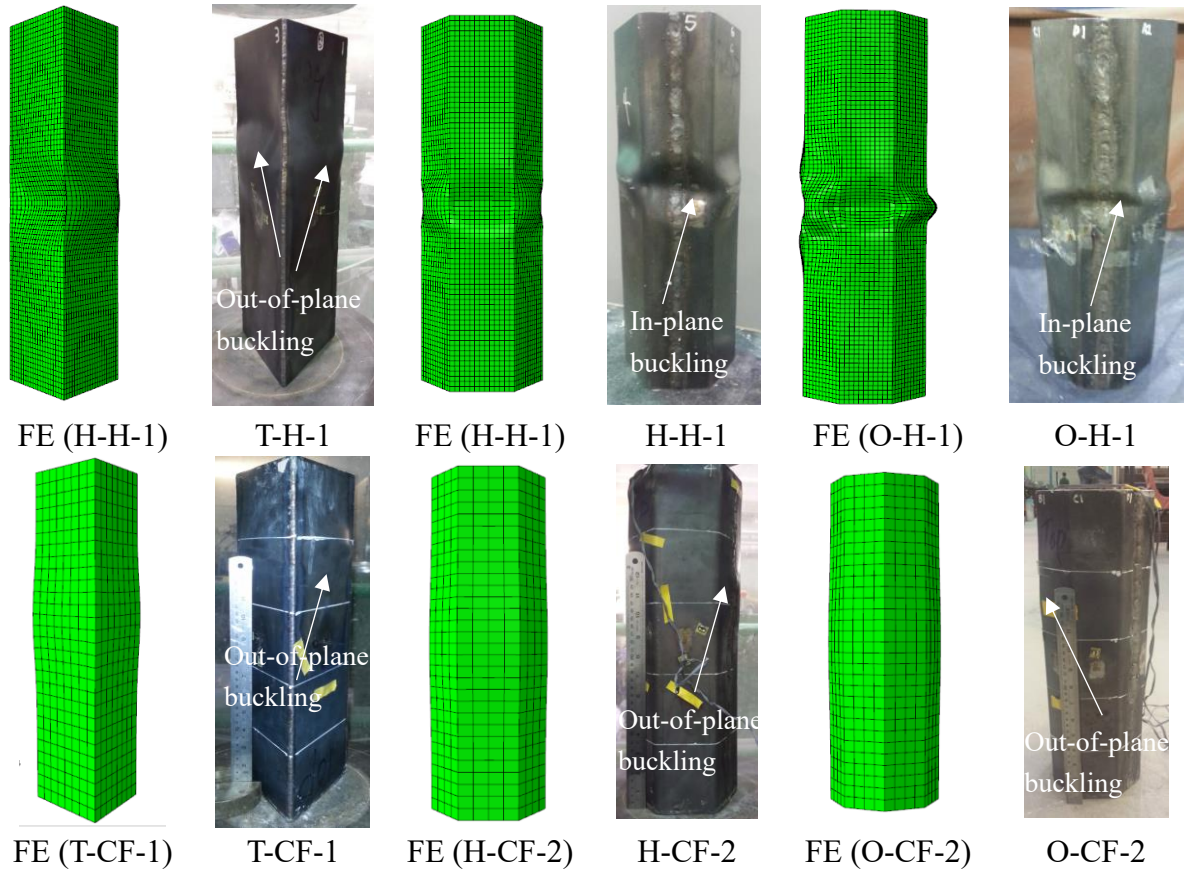

Figure 16. Predictions of failure modes

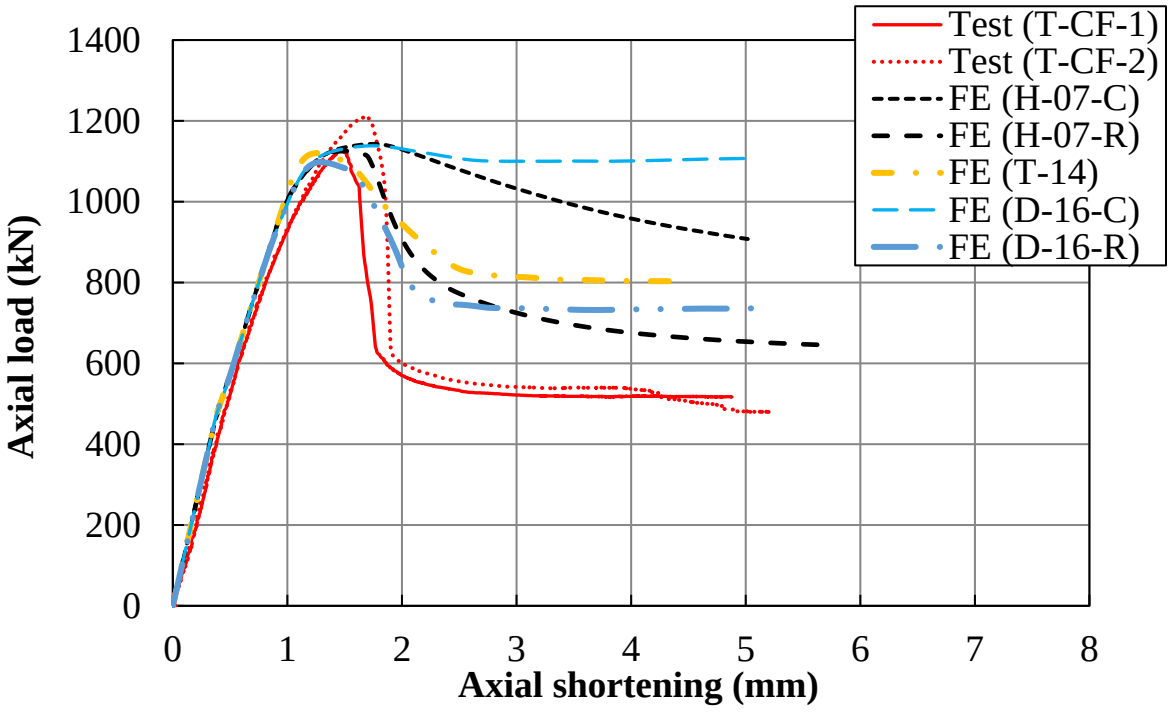

(a) Triangular

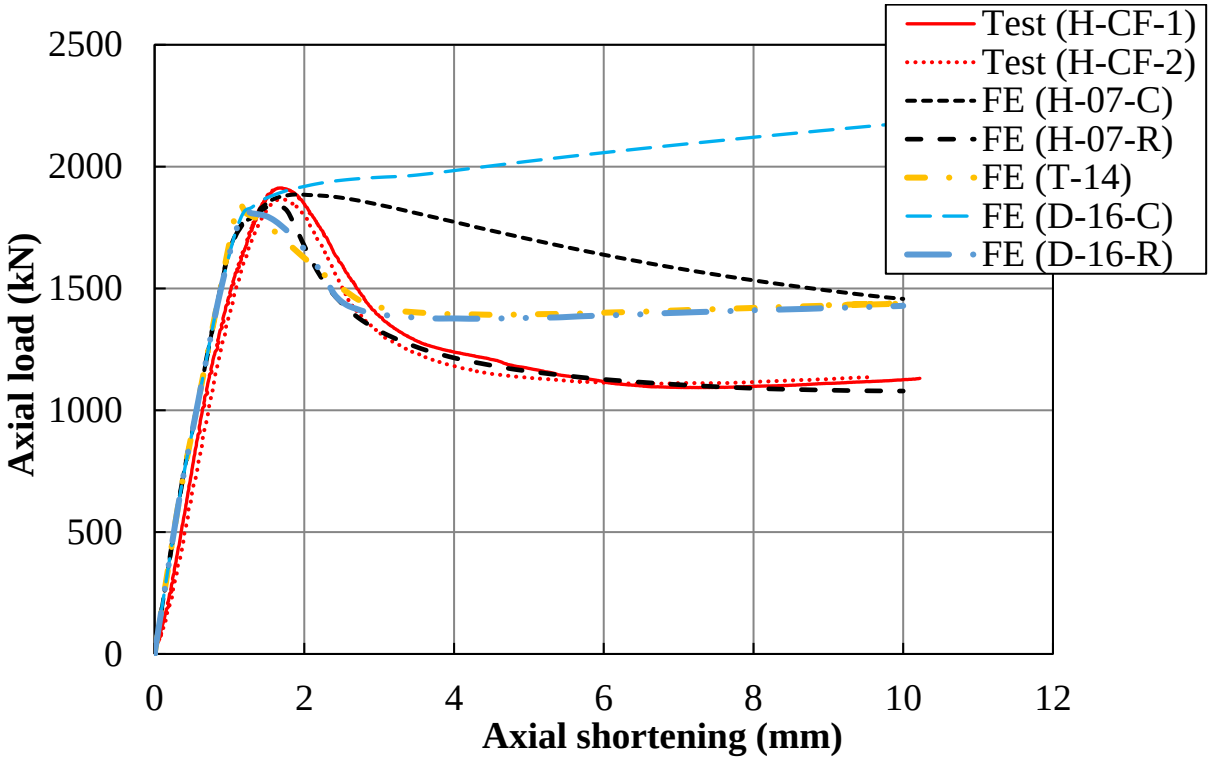

(b) Hexagonal

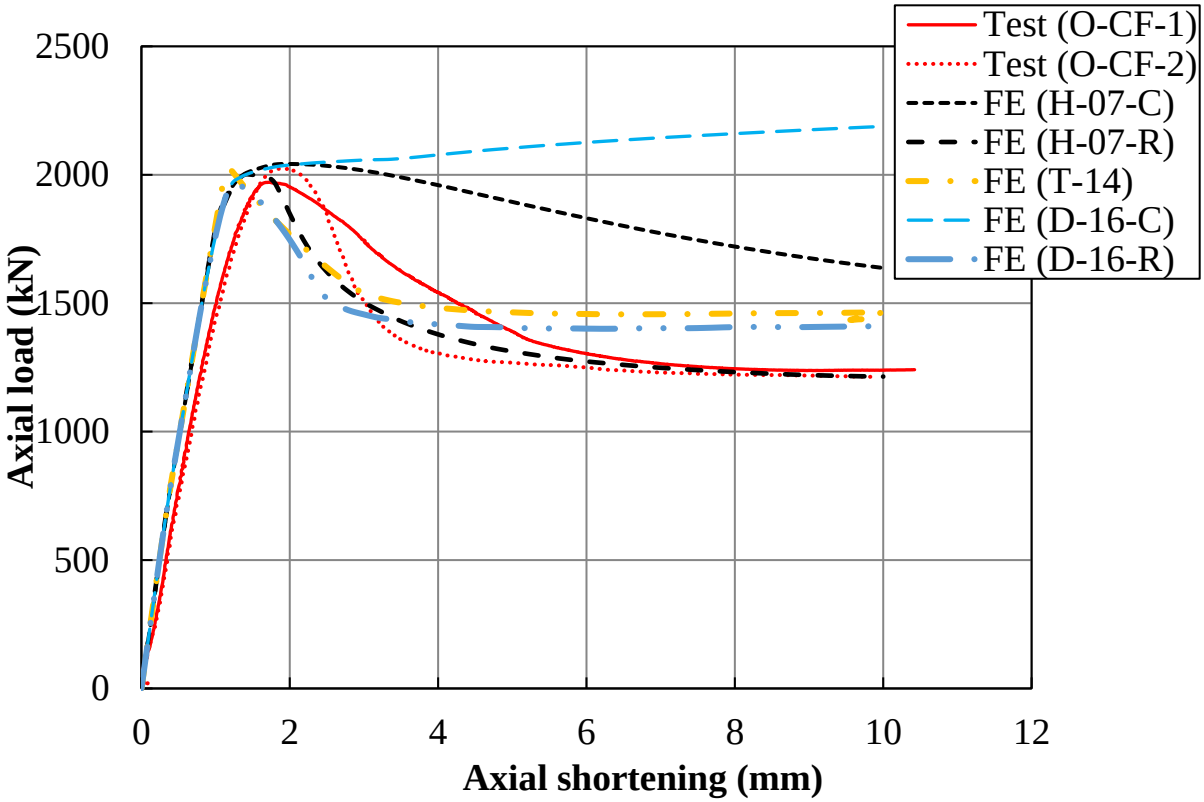

(c) Octagonal

Figure 17. FE predictions of CFSTs